A&A 675, A190 (2023)
https://doi.org/10.1051/0004-6361/202346676

Astronomy & Astrophysics

Deuterium fractionation across the infrared-dark cloud G034.77−00.55 interacting with the supernova remnant W44

G. Cosentino[1], J. C. Tan[1,2], I. Jiménez-Serra[3], F. Fontani[4], P. Caselli[5], J. D. Henshaw[6,7], A. T. Barnes[8], C.-Y. Law[1,8], S. Viti[9,10], R. Fedriani[1,11], C.-J. Hsu[1], P. Gorai[1], and S. Zeng[12]

[1] Department of Space, Earth and Environment, Chalmers University of Technology, 412 96 Gothenburg, Sweden
e-mail: giuliana.cosentino@chalmers.se
[2] Department of Astronomy, University of Virginia, 530 McCormick Road Charlottesville, 22904-4325, USA
[3] Centro de Astrobiología (CSIC/INTA), Ctra. de Torrejón a Ajalvir km 4, Madrid, Spain
[4] INAF Osservatorio Astronomico di Arcetri, Largo E. Fermi 5, 50125 Florence, Italy
[5] Max Planck Institute for Extraterrestrial Physics, Giessenbachstrasse 1, 85748 Garching bei München, Germany
[6] Astrophysics Research Institute, Liverpool John Moores University, 146 Brownlow Hill, Liverpool L3 5RF, UK
[7] Max-Planck-Institut für Astronomie, Königstuhl 17, 69117 Heidelberg, Germany
[8] European Southern Observatory, Karl-Schwarzschild-Strasse 2, 85748 Garching, Germany
[9] Leiden Observatory, Leiden University, PO Box 9513, 2300 RA Leiden, The Netherlands
[10] Department of Physics and Astronomy, University College London, Gower Street, London, WC1E 6BT, UK
[11] Instituto de Astrofísica de Andalucía, CSIC, Glorieta de la Astronomía s/n, 18008 Granada, Spain
[12] Star and Planet Formation Laboratory, Cluster for Pioneering Research, RIKEN, 2-1 Hirosawa, Wako, Saitama, 351-0198, Japan

Received 17 April 2023 / Accepted 31 May 2023

ABSTRACT

Context. Supernova remnants (SNRs) may regulate star formation in galaxies. For example, SNR-driven shocks may form new molecular gas or compress pre-existing clouds and trigger the formation of new stars.
Aims. To test this scenario, we measured the deuteration of N_2H^+, $D_{\rm frac}^{N_2H^+}$ – a well-studied tracer of pre-stellar cores – across the infrared-dark cloud (IRDC) G034.77-00.55, which is known to be experiencing a shock interaction with the SNR W44.
Methods. We use N_2H^+ and N_2D^+ J = 1–0 single pointing observations obtained with the 30m antenna at the Instituto de Radioastronomia Millimetrica to infer $D_{\rm frac}^{N_2H^+}$ towards five positions across the cloud, namely a massive core, different regions across the shock front, a dense clump, and ambient gas.
Results. We find $D_{\rm frac}^{N_2H^+}$ in the range 0.03–0.1, which is several orders of magnitude larger than the cosmic D/H ratio ($\sim 10^{-5}$). The $D_{\rm frac}^{N_2H^+}$ across the shock front is enhanced by more than a factor of 2 ($D_{\rm frac}^{N_2H^+} \sim$ 0.05–0.07) with respect to the ambient gas ($\leq$0.03) and similar to that measured generally in pre-stellar cores. Indeed, in the massive core and dense clump regions of this IRDC we measure $D_{\rm frac}^{N_2H^+} \sim 0.1$.
Conclusions. We find enhanced deuteration of N_2H^+ across the region of the shock, that is, at a level that is enhanced with respect to regions of unperturbed gas. It is possible that this has been induced by shock compression, which would then be indirect evidence that the shock is triggering conditions for future star formation. However, since unperturbed dense regions also show elevated levels of deuteration, further, higher-resolution studies are needed to better understand the structure and kinematics of the deuterated material in the shock region; for example, to decipher whether it is still in a relatively diffuse form or is already organised in a population of low-mass pre-stellar cores.

Key words. astrochemistry – ISM: clouds – ISM: supernova remnants – ISM: individual objects: G34.77-00.55 – ISM: individual objects: W44 – stars: formation

1. Introduction

Infrared-dark clouds (IRDCs) are dense ($n_{\rm H} \geq 10^4$ cm^{-3}; Butler & Tan 2012) and cold ($T \leq 20$ K; Pillai et al. 2006) regions of the interstellar medium (ISM) that have high column densities and extinctions and can therefore appear dark against the diffuse Galactic mid-infrared background. IRDCs are the densest regions of giant molecular clouds (GMCs) and are known to host the formation of low-, intermediate-, and high-mass stars (e.g. Tan et al. 2013; Foster et al. 2014; Pillai et al. 2019; Moser et al. 2020; Yu et al. 2020). Despite their importance for the stellar content of galaxies (e.g. Tan et al. 2014; Hernandez & Tan 2015; Peretto et al. 2016; Retes-Romero et al. 2020; Morii et al. 2021), it is still unclear as to how star formation is initiated therein.

One possible scenario that may lead to the initiation of star formation in IRDCs involves compression due to internal cloud turbulence (e.g. Krumholz & McKee 2005). Another is rooted in the decay of turbulent and/or magnetic support, perhaps associated with the global collapse of a recently formed GMC (e.g. Vázquez-Semadeni et al. 2011). Yet another scenario is characterised by triggered compression by galactic-shear-driven GMC–GMC collisions (Tan 2000), with various numerical simulation studies of this process carried out by for example Tasker & Tan (2009) and Wu et al. (2015, 2017). The involvement of an external agent to a given GMC, such as collision with another GMC, can help explain the large dispersion in star formation activity in GMC populations (e.g. Tan 2000; Lee et al. 2016). Finally, it has also been proposed that IRDC and star formation

are triggered by stellar-feedback-driven shocks, for example in HII regions or supernova remnants (e.g. Inutsuka et al. 2015). In systems like the Milky Way, where the global star formation rate (SFR) is relatively low compared to the amount of dense gas available (Zuckerman & Evans 1974; Krumholz & Tan 2007), stellar-feedback-driven star formation is unlikely to account for the majority of star formation, because if it did, the SFR would grow exponentially to large values. Nevertheless, the process may occur occasionally, and such instances can provide important information; for example, as to whether the star formation process varies when triggered in this way.

There are a number of recent observational studies presenting evidence for instances of IRDC and star formation triggered by SNR-driven shocks (e.g. Cosentino et al. 2019, 2022; Rico-Villas et al. 2020). Cosentino et al. (2019) investigated how the shock driven by the SNR W44 affects the physical conditions of the interacting cloud, the IRDC G034.77-00.55 (hereafter G34.77 or IRDC G from the sample of Butler & Tan 2012). Towards this source, the shock interaction is occurring at the edge of the IRDC, that is, towards an arch-like ridge with no signatures of deeply embedded protostars (Cosentino et al. 2018, 2019; Barnes et al. 2021). Using ALMA images of silicon monoxide (SiO), Cosentino et al. (2019) studied the shocked gas kinematics and inferred a shock velocity of ∼20 km s^{-1}, which is compatible with that previously estimated by Sashida et al. (2013), and a shock dynamical age of $\sim 1.5 \times 10^4$ yr. From C^{18}O observations, the authors estimated a density enhancement – caused by the shock – of a factor of >10; with post-shocked volume densities of $n(H_2) > 10^5$ cm^{-3}.

In this paper, we investigate how the SNR-driven shock may be affecting the chemical properties of the molecular gas. A well-studied tracer of the chemical conditions at the onset of star formation is the fraction of deuterium with respect to hydrogen (D/H) measured from N_2H^+ and N_2D^+ emission (hereafter $D_{\rm frac}^{\rm N_2H^+}$). $D_{\rm frac}^{\rm N_2H^+}$, defined as the ratio of the column densities of the deuterated and non-deuterated species, is highly enhanced in pre-stellar cores (i.e. with values of ∼0.1; Crapsi et al. 2005; Caselli et al. 2008; Emprechtinger et al. 2009) compared to the cosmic D/H abundance (of $\sim 10^{-5}$; Oliveira et al. 2003). This is due to a combination of low temperatures ($T \leq 20$ K) and high densities ($n(H_2) \geq 10^4$ cm^{-3}), which are typical of the pre-stellar phase, and lead to high levels of CO freeze-out onto dust grains (e.g. Caselli et al. 1999). With the CO largely depleted, reactions between N_2 and H_3^+ (and its deuterated form H_2D^+) can efficiently occur, boosting the formation of N_2D^+ (e.g. Dalgarno & Lepp 1984; Caselli et al. 2002; Walmsley et al. 2004). $D_{\rm frac}^{\rm N_2H^+}$ is therefore considered an optimal tracer of the evolutionary phase of both low- and high-mass star forming objects (Fontani et al. 2011; Tan et al. 2013; Giannetti et al. 2019).

Here, we estimate $D_{\rm frac}^{\rm N_2H^+}$ in several regions of the IRDC G34.77. To the best of our knowledge, no previous studies have investigated $D_{\rm frac}^{\rm N_2H^+}$ in shocks driven by SNRs. However, previous studies have measured D/H in other species in shocks associated with molecular outflows (e.g. Codella et al. 2013; Fontani et al. 2014; Busquet et al. 2017). In these environments, the shock passage causes the release into the gas phase of deuterated species whose formation occurs on the icy mantle of dust grains; for example, deuterated counterparts of CH_3OH and H_2CO (Fontani et al. 2014; Busquet et al. 2017). The sputtering and grain–grain collision processes enabled in shocks increase the CO abundance in the gas phase and the formation of N_2D^+ is therefore expected to be suppressed. However, at the high densities reached in the post-shocked gas, gas-phase chemistry can proceed at a much faster rate and the CO depletion timescales can be shortened (Lis et al. 2002, 2016). This may therefore result in enhanced abundances of N_2D^+.

This article is organised as follows. In Sect. 2, we describe the observations and discuss the selection of positions across the cloud. In Sect. 3, we describe the method applied to estimate $D_{\rm frac}^{\rm N_2H^+}$. In Sect. 4, we report and discuss our results. Finally, in Sect. 5, we present our conclusions.

Table 1. Equatorial coordinates of the five positions analysed in this work.

Position	RA(J2000) (hh:mm:ss)	Dec(J2000) (dd:mm:ss)
G3	18:56:48.2	01:23:40
Shock	18:56:42.3	01:23:40
Ridge	18:56:43.4	01:23:28
Clump	18:56:45.2	01:23:52
Ambient	18:56:46.0	01:22:30

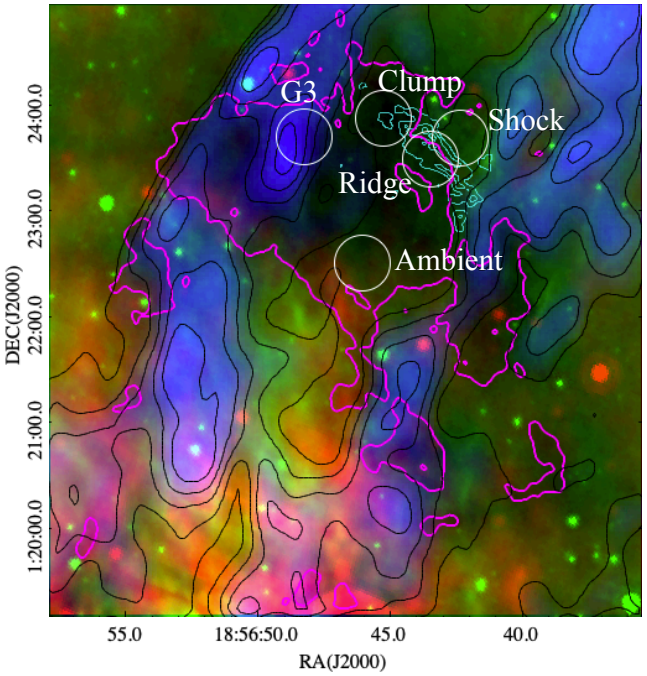

Fig. 1. Three-colour image of G34.77. Red is 24 μm emission (*Spitzer* MIPSGAL; Carey et al. 2009), green is 8 μm emission (*Spitzer* GLIMPSE; Churchwell et al. 2009), and blue is 1 GHz continuum emission (THOR survey; Beuther et al. 2016; black contours from 3 to 27 Jy beam^{-1} by 6 Jy beam^{-1}). The continuum emission probes the gas associated with the expanding shell of the SNR. The magenta contour (A_V = 20 mag Kainulainen & Tan 2013) highlights the cloud shape. Superimposed on the map are the five positions of interest (white circles; 34″ IRAM 30 m beam at the N_2D^+ frequency of 77.112 GHz). The cyan contours correspond to the ALMA SiO contours from Cosentino et al. (2019; from 0.05 to 0.3 Jy beam^{-1} by 0.05 Jy beam^{-1}).

2. Observations and target selection

In March 2020, we observed the $J = 1 \rightarrow 0$ rotational transitions of N_2H^+ and N_2D^+ towards five positions across the IRDC G34.77 (Table 1). These positions (white circles) are shown in Fig. 1 and listed in Table 1. These were selected to probe different environments across G34.77, namely the known massive

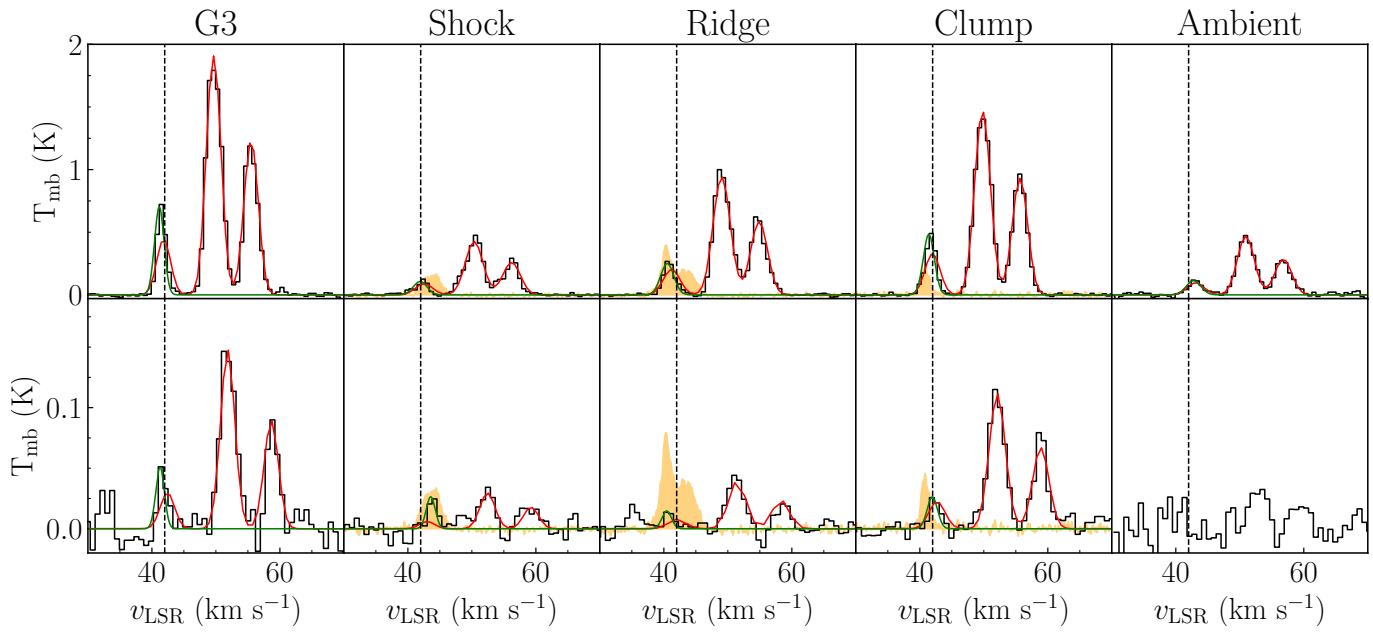

Fig. 2. N_2H^+ (black curves, top panels) and N_2D^+ (black curves, bottom panels) obtained towards the five positions. The IRDC G34.77 central velocity is indicated as a vertical dotted line in all panels. The red curves show the best LTE fitting models obtained by MADCUBA. The green curves show the Gaussian fitting obtained for the isolated component. For the Shock, Ridge, and Clump positions, we report the SiO(2–1) spectra (orange filled) extracted from the ALMA images (Cosentino et al. 2019) towards an angular region consistent with that of our current observations (34″). In the bottom panels, the SiO spectra have been multiplied by 0.2 to allow a more straightforward comparison with the N_2D^+ spectra.

core G3 characterised by Butler & Tan (2012), unperturbed gas within the cloud (referred to here as 'Ambient'), a dense clump adjacent to the shock front ('Clump'; Barnes et al. 2021), and two regions across the shock front seen by ALMA, that is, the 'Shock' and the 'Ridge' (Cosentino et al. 2019). The core G3, first detected as a point-like source, MM4, in the 1.2 mm images presented by Rathborne et al. (2006), shows no evidence of a central protostellar source. This is indicated by the lack of point-like 8 (Rathborne et al. 2006), 24 μm or 4.5 μm (Chambers et al. 2009) sources or SiO emission (Cosentino et al. 2018). Towards the Clump, Barnes et al. (2021) report no evidence of 3 mm continuum and IR emission, indicating that the region is not harbouring deeply embedded protostars. Therefore, G3 and the Clump may be representative of starless regions. However, we note that since 1.2 mm continuum emission is detected towards G3, this may be at an evolutionary stage that is more advanced than the Clump. The Shock position corresponds to the region where the higher velocity shocked material (SiO at ~44–45 km s^{-1}) is found. The Ridge position corresponds to the low-density structure that is almost detached from the main body of the cloud and into which the shock is plunging (SiO at ~39–40 km s^{-1}). Finally, the Ambient position is representative of dense unperturbed material within the IRDC.

Towards the five positions, we used the 30 m single-dish antenna at Instituto de Radioastronomia Millimetrica (IRAM-30 m, Pico Veleta, Spain) to obtain single-pointing N_2H^+(1–0) and N_2D^+(1–0) spectra in position switching mode (off-position RA(J2000) = $18^h57^m01^s$, Dec(J2000) = $1^d22^m25^s$). The angular resolution of the 30 m antenna is 34″ and 27″ at the N_2D^+ and N_2H^+ frequencies, respectively. These correspond to a linear spatial resolution of 0.4–0.5 pc at the distance of G34.77, of namely 2.9 kpc (Rathborne et al. 2006). The FTS spectrometer was used with a frequency resolution of 200 kHz, which corresponds to a velocity resolution of between 0.7 and 0.8 km s^{-1}. Intensities were measured in units of antenna temperature, T_A^*, and converted into main-beam brightness temperature, T_{mb}, using beam and forward efficiencies of 0.81 and 0.95, respectively. The final spectra were produced using the CLASS software within the GILDAS package[1] and have a final velocity resolution of 0.8 km s^{-1}. The achieved rms per channel, σ_{rms}, is 7 and 5 mK for the N_2H^+ and N_2D^+ spectra, respectively.

3. Method

The N_2H^+ (top panels) and N_2D^+ (bottom panels) spectra obtained towards the five positions are shown in Fig. 2. The orange shadows in Fig. 2 correspond to the SiO(2–1) spectra obtained with ALMA in Cosentino et al. (2019). We detect significant N_2H^+ and N_2D^+ emission towards all positions except at the Ambient position, where no N_2D^+ is observed above a threshold of $3 \times A_{rms}$, where $A_{rms} = \sigma_{rms} \times dv \times \sqrt{N_{channel}}$, with dv the velocity resolution of the spectra, and $N_{channel} \simeq 4$ was estimated as the number of channels within a line width of 3 km s^{-1}, which is consistent with that estimated for both the N_2H^+ and N_2D^+ emission (see MADCUBA values in Table 4). We note the presence of additional significant line emission at ~35 km s^{-1} within the N_2D^+ spectrum towards the Ridge. This component shows a line width of ~2.2 km s^{-1} (~3 channels), peak intensity of ~0.018 K, and an integrated intensity of ~0.04 K km s^{-1}, that is, ~$5 \times A_{rms}$. We suggest that this line is either due to emission present along the line of sight or to an unknown species.

From the shown spectra, we estimate $D_{frac}^{N_2H^+}$ as:

$$D_{frac}^{N_2H^+} = \frac{N(N_2D^+)}{N(N_2H^+)}, \quad (1)$$

where $N(N_2D^+)$ and $N(N_2H^+)$ are the total column densities of these species. To estimate these quantities, we use the software

[1] See http://www.iram.fr/IRAMFR/GILDAS

MADCUBA[2] (Martín et al. 2019) to fit the hyper-fine structure of the two species. By comparing the line emission with local thermodynamic equilibrium (LTE) models, MADCUBA provides estimates of the species excitation temperature, T_{ex}, column density, N, centroid velocity, v_{LSR}, and line width, Δv. Initially, we fit the N_2D^+ and N_2H^+ spectra with just one assumption, namely that the emission fills the beam (filling factor = 1). However, the software is unable to produce reasonable models, as indicated by the high uncertainties in the returned parameters (>200%). This is likely due to the presence of a complex kinematic structure that is not well resolved at the velocity resolution of our observations (0.8 km s^{-1}). We therefore conclude that it is not possible to estimate the excitation temperatures of the two species from a single rotational transition, and assume all lines to have the same T_{ex} = 9 K, as measured from multiple CH_3OH transitions detected towards the shock peak in G34.77 (Cosentino et al. 2018). How this assumption affects our results is discussed in Appendix A.

The best LTE fitting models are shown in Fig. 2 (red curves) for the five regions. In Table 3, $N(N_2D^+)$ and $N(N_2H^+)$ are reported together with the corresponding $D_{frac}^{N_2H^+}$ values and the *Herschel*-derived mass surface densities, Σ, towards the five positions (Lim et al. 2016). The *Herschel*-derived image has an angular resolution of 18″, but the Σ values listed in Table 3 were extracted from a region with a 34″ aperture, consistent with that of the N_2D^+ observations.

We also estimate the N_2H^+ and N_2D^+ column densities from Eq. (2), which is Eq. (A4) from Caselli et al. (2002), under the assumption of optically thin emission:

$$N = \frac{8\pi\nu^2}{A_{ul}g_u c^3}\frac{k}{h}\frac{Q_{rot}}{1-\exp(-h\nu/kT_{ex})}\times\frac{\exp(E_l/(kT_{ex}))}{J_\nu(T_{ex})-J_\nu(T_{bg})}\times W_{tot}, \quad (2)$$

with the partition function, Q_{rot}, defined as:

$$Q_{rot} = \sum_{J=1}^{\infty}(2J+1)\exp\left(\frac{-E_J}{kT_{ex}}\right). \quad (3)$$

In Eqs. (2) and (3), ν is the line frequency, A_{ul} is the Einstein coefficient for spontaneous emission and g_{up} is the statistical weight of the upper state. $J_\nu(T_{ex})$ and $J_\nu(T_{bg})$ are the equivalent Rayleigh-Jeans excitation and background temperatures (T_{bg} = 2.73 K), that is $J_\nu(T) = (h\nu/k)[\exp(h\nu/kT)-1]^{-1}$. J is the rotational state quantum number and $E_J = J(J+1)hB$ the corresponding state energy, which is calculated from the molecular rotational constant B. W_{tot} is the integrated intensity of the full rotational transition J = 1–0. Finally, T_{ex} is the line excitation temperature. The spectroscopic quantities for the two species were obtained from the CDMS catalogue[3] and are reported in Table 2.

We performed Gaussian fittings of the N_2H^+ and N_2D^+ isolated components and calculated the integrated intensity, $W_{isolated}$, as the area underneath the Gaussian. We then estimate W_{tot} by scaling $W_{isolated}$ for its relative intensity R_i = 1/9. The best Gaussian fitting are reported in Fig. 2 (green curves), while Table 3 lists the N_2H^+ and N_2D^+ column densities obtained from Eq. (2) whilst assuming T_{ex} = 9 K (Cosentino et al. 2018) and the associated $D_{frac}^{N_2H^+}$ values. The best-fitting parameters obtained with both the MADCUBA and Gaussian fitting analysis are reported in Table 4.

[2] MADCUBA is a software developed in the Madrid Center of Astrobiology (INTA-CSIC). https://cab.inta-csic.es/madcuba/

[3] See https://cdms.astro.uni-koeln.de/classic/

Table 2. Spectroscopic information of the targeted species as obtained from the CDMS catalogue.

Species	Frequency (GHz)	E_{up} (K)	g_{up}	A_{ul} (10^{-5} s^{-1})	B (MHz)
N_2D^+	77.109	3.70	3	2.06	38 554.719
N_2H^+	93.173	4.47	3	3.63	46 586.867

From Table 3, the $D_{frac}^{N_2H^+}$ values obtained from the two methods (MADCUBA and Gaussian fitting of isolated components) are in agreement. The only significant discrepancy is found towards the Shock, where the $D_{frac}^{N_2H^+}$ value estimated from the Gaussian fitting method (~0.2) is a factor of 3 larger than that obtained from the MADCUBA analysis (~0.07). Towards this position, the ratio between the intensity of the main and isolated N_2D^+ components is smaller (~1.2) than that seen towards other positions (~4.5). As a consequence, the N_2D^+ isolated component towards the Shock is not well reproduced by MADCUBA. This could be due to the isolated component being affected by a random noise spike that coincides with the line position, making it appear enhanced. Alternatively, the N_2D^+ emission towards the Ridge may need a non-LTE approach, for which the collisional coefficients of N_2D^+ are not available and multiple rotational transitions are needed. Finally, we exclude the possibility that the N_2D^+ is blended with another molecular species as no other molecular transitions are found at these frequencies.

Finally, in addition to the statistical uncertainty reported by MADCUBA for the N_2H^+ and N_2D^+ column densities, we also consider the systematic uncertainty due to the assumption T_{ex} = 9 K. A ± 30% variation of T_{ex}, that is variation within the range of 6–12 K, would result in a 5–10% variation of the N_2H^+ column density and 3–10% in the N_2D^+ column densities. Hence, we assume a systematic uncertainty of 10% and add this in quadrature to the statistical errors. The obtained total uncertainties on the column density values are then propagated – with standard Gaussian rules – in order to estimate the uncertainties on $D_{frac}^{N_2H^+}$. The final values are reported in Table 3.

4. Results and discussion

Towards all positions, we obtain D/H values that are several orders of magnitude larger than the cosmic D/H abundance. We find $D_{frac}^{N_2H^+}$ in the range ~0.05–0.1 towards G3, the Shock, the Ridge, and the Clump. For the Ambient gas, we estimate an upper limit of 0.03. These results are shown in Fig. 3, where we compare the obtained $D_{frac}^{N_2H^+}$ estimates with those typically observed in low-mass starless cores (LMSCs; Crapsi et al. 2005; Fontani et al. 2006; Friesen et al. 2013; Cheng et al. 2021), high-mass starless cores (HMSCs; Fontani et al. 2011; Kong et al. 2016), high-mass protostellar objects (HMPOs; Fontani et al. 2011), low-mass protostellar objects (LMPOs; Emprechtinger et al. 2009; Friesen et al. 2013) and large-scale regions of IRDCs (Miettinen et al. 2011; Gerner et al. 2015; Barnes et al. 2016).

In Fig. 4, we show $D_{frac}^{N_2H^+}$ as a function of mass surface density, Σ. From Fig. 4 and Table 3, the Shock and Ridge show an Σ value that is lower than or similar to that found for the Ambient region. Hence, $D_{frac}^{N_2H^+}$ would be expected to be lower than or comparable to that measured towards the Ambient region. However, an opposite trend is seen in Fig. 4. Towards the Shock, the $N(N_2H^+)$ is similar to that estimated for the Ambient gas, but the $N(N_2D^+)$ is enhanced by at least a factor of 2. Towards the

Table 3. Mass surface density (Σ), N_2H^+ and N_2D^+ column densities and deuterium fraction, $D_{frac}^{N_2H^+}$, of the five positions analysed in this work using both the MADCUBA software and Gaussian fittings of the isolated components.

Position	Σ	MADCUBA			Gaussian fitting		
		$N(N_2H^+)$	$N(N_2D^+)$	$D_{frac}^{N_2H^+}$	$N(N_2H^+)$	$N(N_2D^+)$	$D_{frac}^{N_2H^+}$
	(g cm^{-2})	(10^{13} cm^{-2})	(10^{12} cm^{-2})		(10^{13} cm^{-2})	(10^{12} cm^{-2})	
G3	0.09	1.47±0.2	1.33±0.2	0.090±0.02	1.55±0.16	1.4±0.2	0.09±0.01
Shock	0.04	0.36±0.09	0.26±0.1	0.07±0.03	0.34±0.04	0.7±0.2	0.22±0.06
Ridge	0.05	0.80±0.2	0.42±0.1	0.053±0.02	0.77±0.09	0.4±0.1	0.05±0.01
Clump	0.07	1.17±0.1	1.14±0.1	0.097±0.02	1.24±0.13	0.9±0.2	0.07±0.02
Ambient	0.06	0.40±0.09	≤0.1	≤0.03	0.38±0.01	≤0.1	≤0.03

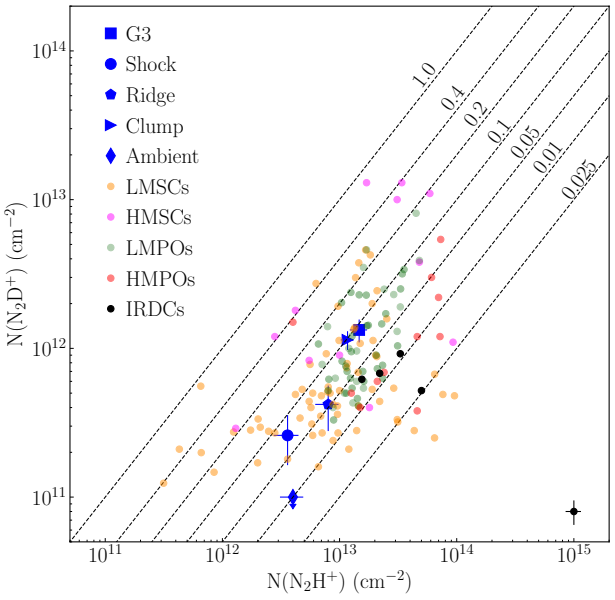

Fig. 3. Column density values from the MADCUBA analysis of N_2D^+ as a function of N_2H^+ for all the positions analysed in this work, as well as literature values for LMSCs (Crapsi et al. 2005; Fontani et al. 2006; Friesen et al. 2013; Cheng et al. 2021), HMSCs (Fontani et al. 2011; Kong et al. 2016), HMPOs (Fontani et al. 2011), LMPOs (Emprechtinger et al. 2009; Friesen et al. 2013), and IRDCs (Miettinen et al. 2011; Gerner et al. 2015; Barnes et al. 2016). The average uncertainties associated to the data point from the literature are reported in the bottom right corner. Finally, dotted lines correspond to fixed values of D/H ratios.

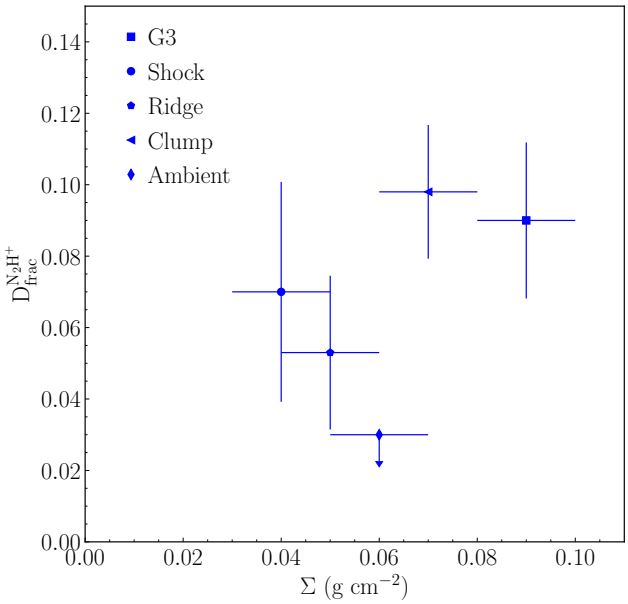

Fig. 4. $D_{frac}^{N_2H^+}$ obtained from the MADCUBA analysis as function of Σ. Different symbols correspond to different positions. The uncertainty on the Σ values is 0.01 g cm^{-2}, as reported by Lim et al. (2016).

Ridge, the N_2H^+ column density is significantly larger than that reported towards the Ambient gas within the uncertainties, indicating the presence of more dense material towards this region. At the same time, the N_2D^+ column density towards this position is more than a factor of ∼3 larger than that measured for the Ambient gas. As a consequence, $D_{frac}^{N_2H^+}$ towards the two positions is enhanced (but within the uncertainty) with respect to the unperturbed gas within the cloud. These differences indicate that, towards the Shock and the Ridge, additional processes may be boosting the production of D-bearing species with respect to the unperturbed Ambient gas.

This enhanced $D_{frac}^{N_2H^+}$ may be produced in the fast-cooling post-shocked gas, where the shock has compressed the gas to densities of $n(H_2) > 10^5$ cm^{-3}. This high density is expected to shorten the CO depletion timescale and boost the production of N_2D^+ (Lis et al. 2002, 2016). For the post-shocked density $n(H_2) \geq 10^5$ cm^{-3} measured in Cosentino et al. (2019), the CO depletion timescale is expected to be ≤10^4 yr (Caselli et al. 1999), which is consistent with the shock dynamical age (Cosentino et al. 2019). On the other hand, as reported by Codella et al. (2013) towards the molecular outflow shock L1157-B1, N_2H^+ is expected to be a fossil record of the pre-shocked gas that has been compressed. These two effects together result in an enhanced $D_{frac}^{N_2H^+}$ towards the Shock and the Ridge. In accordance with this scenario, the CO depletion factor towards the two positions is in the range of ∼4–6. We obtained CO depletion maps obtained towards G34.77 using ^{13}CO(1–0) and C^{18}O(1–0) emission maps from the Green Bank Telescope and these will be presented in a forthcoming paper (Petrova et al., in prep.). We converted the ^{13}CO(1–0) and C^{18}O(1–0) maps into column densities assuming an excitation temperature of 7.5 K and using the mass surface density maps derived from *Herschel* data (Lim et al. 2016).

Finally, both the N_2H^+ and N_2D^+ centroid velocities towards the Ridge (Table 4) are consistent with the velocity of the post-shocked gas (∼40 km s^{-1}; Cosentino et al. 2019). Toward the Shock, both the N_2H^+ and N_2D^+ emission show higher velocities of ∼42 km s^{-1}, but this still consistent with the lowest velocities (which are associated with the most downstream post-shocked gas) reached by the SiO towards that region (Fig. 2). We note

Table 4. Best-fitting parameters of the N_2H^+ and N_2D^+ emission lines obtained using MADCUBA and the Gaussian fitting of the isolated components.

	MADCUBA				Gaussian fitting					
	N_2H^+		N_2D^+		N_2H^+			N_2D^+		
Position	v_0 (km s^{-1})	Δv (km s^{-1})	v_0 (km s^{-1})	Δv (km s^{-1})	v_0 (km s^{-1})	Δv (km s^{-1})	T_{peak} (K)	v_0 (km s^{-1})	Δv (km s^{-1})	T_{peak} (K)
G3	41.50±0.04	2.5±0.1	41.8±0.1	2.6±0.2	41.2	1.7	0.70	41.3	1.6	0.05
Shock	42.21± 0.05	3.2±0.1	42.3±0.2	2.7±0.5	41.9	2.6	0.11	43.6	1.6	0.03
Ridge	40.89± 0.04	3.1±0.1	41.4±0.2	3.1±0.4	40.5	2.4	0.25	40.4	1.6	0.02
Clump	41.67± 0.03	2.8±0.1	42.08±0.04	3.0±0.1	41.4	2.1	0.48	41.9	1.9	0.03
Ambient	42.79± 0.03	3.1±0.1	···	···	42.8	2.6	0.11	···	···	···

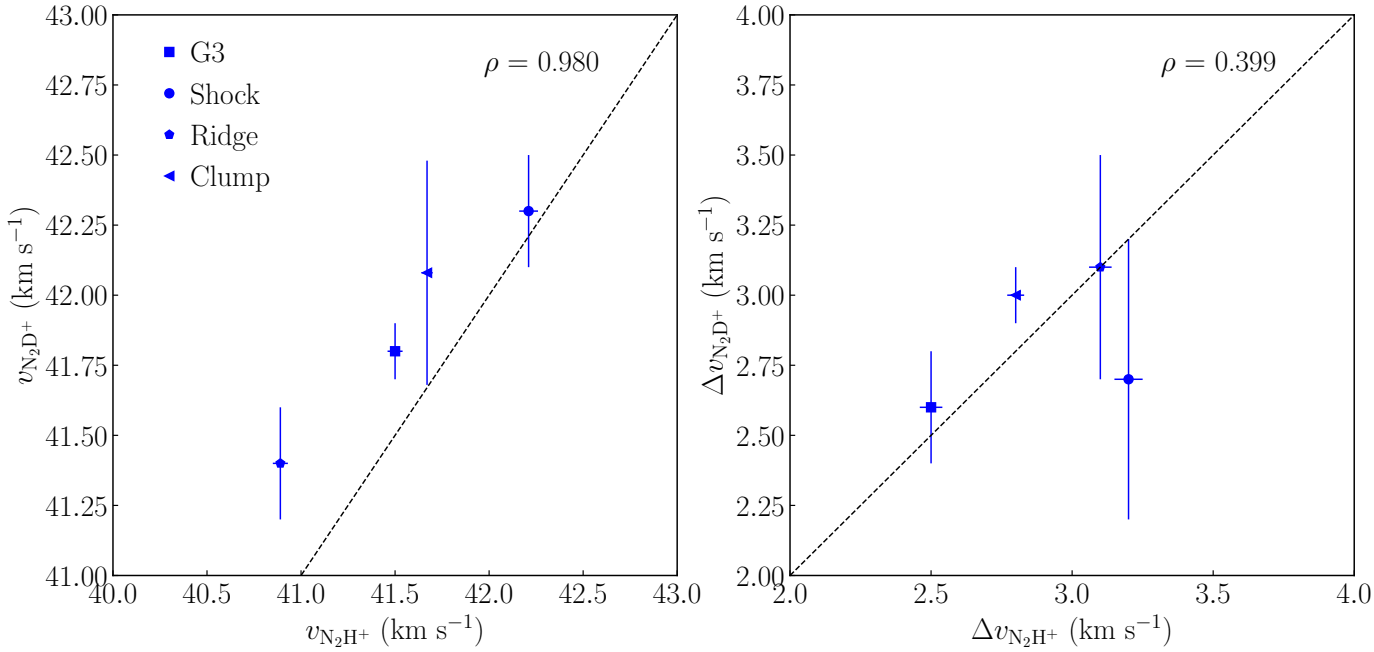

Fig. 5. N_2D^+ centroid velocities (left) and line widths (right) as a function of the corresponding N_2H^+ quantities. The Pearson's correlation coefficients are indicated within each panel.

that the N_2H^+ column density towards the Ridge is a factor 1.5 larger than that measured towards the Shock. This may simply reflect the decreasing amount of dense gas at the cloud outskirts (from the Ridge to the Shock) and/or a larger compression of the gas towards the Ridge. Indeed, here the shock velocities probed by SiO reach even lower values (down to 39 km s^{-1}; Cosentino et al. 2019).

The high $D_{frac}^{N_2H^+}$ across the shock front may also be explained by the presence of a population of starless cores. In this parallel scenario, we speculate that the denser cooled-down post-shocked material is not diffuse but is rather organised into low-mass cores, whose formation may have been triggered by the shock passage that compresses gas to high densities (Cosentino et al. 2019).

Furthermore, as shown in Fig. 4, the $D_{frac}^{N_2H^+}$ estimates towards the Shock (blue circle) and the Ridge (blue plus) are consistent with those previously measured towards LMSCs (orange circles Crapsi et al. 2005; Fontani et al. 2006; Friesen et al. 2013) and LMPOs (Emprechtinger et al. 2009; Friesen et al. 2013, green circles). However, as no evidence of deeply embedded protostars has been found towards these regions (Cosentino et al. 2019; Barnes et al. 2021), we exclude the possibility that this putative low-mass population could have already reached the protostellar phase.

We note that the timescale required for a core to reach $D_{frac}^{N_2H^+} \sim 0.1$ may be as short as 10^4 yr (Kong et al. 2015) under the physical conditions of density and cosmic ionisation rate similar to those estimated towards the shock in G34.77 ($n(H_2) \sim 10^5$ cm^{-3} and $\zeta \sim 10^{-15}$ s^{-1}; Cosentino et al. 2019) and if the H_2 ortho-to-para (OPR) ratio is ≤0.1. However, at the relatively low angular resolution of our observations, it is not possible to distinguish between the two scenarios described above, namely of cooled-down diffuse post-shocked gas or a population of low-mass pre-stellar cores.

Towards the Clump, we measure $D_{frac}^{N_2H^+} \sim 0.09$, which is consistent with that measured towards G3 and previously reported towards LMSC, HMSCs, and LMPOs (Fig. 3). The Clump also has a relatively high mass surface density of 0.07 g cm^{-1} (~60 $M_\odot$ within the 34″ beam), which is consistent with that of G3. Towards this position, Barnes et al. (2021) report a N_2H^+ emission peak. As the source shows no signatures of point-like emission at 4.5, 8, or 24 μm (Chambers et al. 2009) nor 1 mm

(Rathborne et al. 2006) or 3 mm continuum emission (Cosentino et al. 2019; Barnes et al. 2021), we exclude that the Clump may be hosting deeply embedded protostars. Due to its mass, density, lack of IR and mm continuum signatures, and high $D_{\rm frac}^{\rm N_2H^+}$ value, we speculate that the Clump may still be evolving into the state of a centrally condensed pre-stellar core. However, it remains to be established whether or not the gas is gravitationally bound or whether or not it will fragment. We note that the Clump is located in the immediate vicinity of the shock front, where the shocked gas seen in SiO (Fig. 1) has already decelerated down to 40 km s^{-1}. However, the N_2H^+ and N_2D^+ centroid velocities are not consistent with that of the post-shocked material. They indeed appear more in agreement with those measured towards the inner cloud, that is, G3. We therefore speculate that the Clump may have existed before the interaction with the SNR and has only been marginally affected by the shock.

The N_2H^+ and N_2D^+ line profiles

Table 4 shows the N_2H^+ and N_2D^+ centroid velocities, line widths (full width at half maximum) and line peaks obtained from the MADCUBA analysis and the Gaussian fitting method, respectively. The two sets of parameters agree within the velocity resolution of our observations (0.8 km s^{-1}). Figure 5 shows the correlation plots between the N_2H^+ and N_2D^+ centroid velocities (left) and line width (right) obtained from the MADCUBA analysis. We see that the centroid velocities of the two species are in agreement within the 0.8 km s^{-1} velocity resolution. This is also the case for the line widths of the species. The only exception may be represented by the Shock, where the N_2H^+ emission is slightly broader (3.2 km s^{-1}) than the corresponding N_2D^+ emission (2.7 km s^{-1}). In the proposed scenarios, this may be due to the fact that the N_2H^+ also probes gas in the act of being compressed, while the N_2D^+ does not. These putative complex kinematics are marginally seen in the velocity wings in the N_2H^+ spectrum, but cannot be fully resolved at the current velocity resolution. The presence of this additional unresolved N_2H^+ velocity component would result in the N_2H^+ column density being slightly overestimated. Therefore, the $D_{\rm frac}^{\rm N_2H^+}$ towards the Shock may be even larger than what is reported.

5. Conclusions

We report observations of the N_2H^+ and N_2D^+ $J = 1-0$ emission towards five positions across the IRDC G34.77, namely a massive core (G3; 'Core'), different positions across the shock front driven by the nearby SNR W44 ('Shock' and 'Ridge'), a dense clump ('Clump'), and unperturbed cloud material ('Ambient'). We measured $D_{\rm frac}^{\rm N_2H^+}$ across the cloud and compared the obtained results with those typically measured in star-forming regions at different evolutionary stages. We find that towards the Core, Shock, Ridge, and Clump, $D_{\rm frac}^{\rm N_2H^+}$ is significantly larger than that measured towards the Ambient region ($D_{\rm frac}^{\rm N_2H^+} \leq 0.03$) and is several orders of magnitude greater than the cosmic D/H ratio. We report enhanced $D_{\rm frac}^{\rm N_2H^+}$ towards both the Shock and the Ridge, where the gas is being compressed by the SNR-driven shock. Towards these regions, we suggest that the N_2H^+ emission may be a fossil record of the pre-shocked material that is now being compressed by the shock passage. We also suggest that the enhanced N_2D^+ column densities – with respect to the Ambient region – towards these regions may be associated with the fast-cooling, much denser post-shocked material. Here, the previously reported high densities enable a faster chemistry that quickly causes CO to be depleted and boosts the formation of D-bearing species in the gas phase. We also speculate that the shock passage may have triggered the formation of a low-mass starless core population in the dense post-shocked material. Here, the measured $D_{\rm frac}^{\rm N_2H^+}$ may be produced towards these cores. High-angular resolution images are necessary to distinguish between the possible scenarios. Finally, we measured $D_{\rm frac}^{\rm N_2H^+} \sim 0.1$ towards the Clump, which is similar to that observed towards starless cores, including G3. The source also has a mass surface density similar to that typically observed in clumps with the potential to harbour star formation. We speculate that this clump may represent a starless core in the making but we find no evidence that this formation was triggered by the shock passage.

Acknowledgements. G.C. acknowledges support from the Swedish Research Council (VR Grant; Project: 2021-05589). J.C.T. acknowledges support from ERC project 788829–MSTAR. I.J-.S acknowledges funding from grant No. PID2019-105552RB-C41 awarded by the Spanish Ministry of Science and Innovation/State Agency of Research MCIN/AEI/10.13039/501100011033. J.D.H. gratefully acknowledges financial support from the Royal Society (University Research Fellowship; URF/R1/221620). P.G. acknowledges support from the Chalmers Cosmic Origins postdoctoral fellowship. R.F. acknowledges funding from the European Union's Horizon 2020 research and innovation programme under the Marie Sklodowska-Curie grant agreement No 101032092. R.F. also acknowledges support from the grants Juan de la Cierva FJC2021-046802-I, PID2020-114461GB-I00 and CEX2021-001131-S funded by MCIN/AEI/ 10.13039/501100011033 and by "European Union NextGenerationEU/PRTR". S.V. acknowledges partial funding from the European Research Council (ERC) Advanced Grant MOPPEX 833460. S.V. and J.C.T acknowledge the support from a Royal Society International Exchanges Scheme grant (IES\R3\170325)

References

Barnes, A. T., Kong, S., Tan, J. C., et al. 2016, MNRAS, 458, 1990
Barnes, A. T., Henshaw, J. D., Fontani, F., et al. 2021, MNRAS, 503, 4601
Beuther, H., Bihr, S., Rugel, M., et al. 2016, A&A, 595, A32
Busquet, G., Fontani, F., Viti, S., et al. 2017, A&A, 604, A20
Butler, M. J., & Tan, J. C. 2012, ApJ, 754, 5
Carey, S. J., Noriega-Crespo, A., Mizuno, D. R., et al. 2009, PASP, 121, 76
Caselli, P., Walmsley, C. M., Tafalla, M., Dore, L., & Myers, P. C. 1999, ApJ, 523, L165
Caselli, P., Benson, P. J., Myers, P. C., & Tafalla, M. 2002, ApJ, 572, 238
Caselli, P., Vastel, C., Ceccarelli, C., et al. 2008, A&A, 492, 703
Chambers, E. T., Jackson, J. M., Rathborne, J. M., & Simon, R. 2009, ApJS, 181, 360
Cheng, Y., Tan, J. C., Caselli, P., et al. 2021, ApJ, 916, 78
Churchwell, E., Babler, B. L., Meade, M. R., et al. 2009, PASP, 121, 213
Codella, C., Viti, S., Ceccarelli, C., et al. 2013, ApJ, 776, 52
Cosentino, G., Jiménez-Serra, I., Henshaw, J. D., et al. 2018, MNRAS, 474, 3760
Cosentino, G., Jiménez-Serra, I., Caselli, P., et al. 2019, ApJ, 881, L42
Cosentino, G., Jiménez-Serra, I., Tan, J. C., et al. 2022, MNRAS, 511, 953
Crapsi, A., Caselli, P., Walmsley, C. M., et al. 2005, ApJ, 619, 379
Dalgarno, A., & Lepp, S. 1984, ApJ, 287, L47
Emprechtinger, M., Caselli, P., Volgenau, N. H., Stutzki, J., & Wiedner, M. C. 2009, A&A, 493, 89
Fontani, F., Caselli, P., Crapsi, A., et al. 2006, A&A, 460, 709
Fontani, F., Palau, A., Caselli, P., et al. 2011, A&A, 529, L7
Fontani, F., Sakai, T., Furuya, K., et al. 2014, MNRAS, 440, 448
Foster, J. B., Arce, H. G., Kassis, M., et al. 2014, ApJ, 791, 108
Friesen, R. K., Kirk, H. M., & Shirley, Y. L. 2013, ApJ, 765, 59
Gerner, T., Shirley, Y. L., Beuther, H., et al. 2015, A&A, 579, A80
Giannetti, A., Bovino, S., Caselli, P., et al. 2019, A&A, 621, L7
Hernandez, A. K., & Tan, J. C. 2015, ApJ, 809, 154
Inutsuka, S.-i., Inoue, T., Iwasaki, K., & Hosokawa, T. 2015, A&A, 580, A49
Kainulainen, J., & Tan, J. C. 2013, A&A, 549, A53
Kong, S., Caselli, P., Tan, J. C., Wakelam, V., & Sipilä, O. 2015, ApJ, 804, 98
Kong, S., Tan, J. C., Caselli, P., et al. 2016, ApJ, 821, 94
Krumholz, M. R., & McKee, C. F. 2005, ApJ, 630, 250
Krumholz, M. R., & Tan, J. C. 2007, ApJ, 654, 304
Lee, E. J., Miville-Deschênes, M.-A., & Murray, N. W. 2016, ApJ, 833, 229
Lim, W., Tan, J. C., Kainulainen, J., Ma, B., & Butler, M. 2016, AAS Meeting Abstracts, 227, 424.06

Lis, D. C., Gerin, M., Phillips, T. G., & Motte, F. 2002, ApJ, 569, 322
Lis, D. C., Wootten, H. A., Gerin, M., et al. 2016, ApJ, 827, 133
Martín, S., Martín-Pintado, J., Blanco-Sánchez, C., et al. 2019, A&A, 631, A159
Miettinen, O., Hennemann, M., & Linz, H. 2011, A&A, 534, A134
Morii, K., Sanhueza, P., Nakamura, F., et al. 2021, ApJ, 923, 147
Moser, E., Liu, M., Tan, J. C., et al. 2020, ApJ, 897, 136
Oliveira, C. M., Hébrard, G., Howk, J. C., et al. 2003, ApJ, 587, 235
Peretto, N., Lenfestey, C., Fuller, G. A., et al. 2016, A&A, 590, A72
Pillai, T., Wyrowski, F., Carey, S. J., & Menten, K. M. 2006, A&A, 450, 569
Pillai, T., Kauffmann, J., Zhang, Q., et al. 2019, A&A, 622, A54
Punanova, A., Caselli, P., Pon, A., Belloche, A., & André, P. 2016, A&A, 587, A118
Rathborne, J. M., Jackson, J. M., & Simon, R. 2006, ApJ, 641, 389
Retes-Romero, R., Mayya, Y. D., Luna, A., & Carrasco, L. 2020, ApJ, 897, 53
Rico-Villas, F., Martín-Pintado, J., González-Alfonso, E., Martín, S., & Rivilla, V. M. 2020, MNRAS, 491, 4573
Sashida, T., Oka, T., Tanaka, K., et al. 2013, ApJ, 774, 10
Tan, J. C. 2000, ApJ, 536, 173
Tan, J. C., Kong, S., Butler, M. J., Caselli, P., & Fontani, F. 2013, ApJ, 779, 96
Tan, J. C., Beltrán, M. T., Caselli, P., et al. 2014, in Protostars and Planets VI, eds. H. Beuther, R. S. Klessen, C. P. Dullemond, & T. Henning (Tucson: University of Arizona Press), 149
Tasker, E. J., & Tan, J. C. 2009, ApJ, 700, 358
Vázquez-Semadeni, E., Banerjee, R., Gómez, G. C., et al. 2011, MNRAS, 414, 2511
Walmsley, C. M., Flower, D. R., & Pineau des Forêts, G. 2004, A&A, 418, 1035
Wu, B., Van Loo, S., Tan, J. C., & Bruderer, S. 2015, ApJ, 811, 56
Wu, B., Tan, J. C., Nakamura, F., et al. 2017, ApJ, 835, 137
Yu, H., Wang, J., & Tan, J. C. 2020, ApJ, 905, 78
Zuckerman, B., & Evans, N. J., I. 1974, ApJ, 192, L149

Appendix A: The HFS GILDAS fitting method

The HFS method in GILDAS is a fitting procedure that reproduces the N_2H^+ and N_2D^+ hyperfine structures in the regime of optically thin and thick lines. In the case of optically thick lines, the excitation temperature can be estimated together with the total line optical depth and the centroid velocity. We applied the HFS method to the N_2H^+ and N_2D^+ spectra in Figure 2. For all the N_2D^+ spectra, the HFS method indicates that the lines are optically thin towards all positions. It is therefore not possible to estimate T_{ex} for this species. For the N_2H^+ spectra, the HFS method indicates optically thin lines towards all position except the core G3. Furthermore, towards the Shock, Ridge and Clump, the method also returns a poor fit. This is likely due to the presence of a complex kinematic structures not resolved at the low velocity resolution of our observations. As a consequence, it is not possible to estimate T_{ex} of N_2H^+ towards these positions. The only spectrum for which the HFS is successful is the N_2H^+ emission towards the core G3, for which we report the best fitting parameters in Table A.1.

Position (GHz)	$T_A \times \tau$ (K)	v_{lsr} (km s^{-1})	Δv (km s^{-1})	τ_{main}
G3	5.5±0.1	41.600±0.005	2.1±0.1	1.48±0.1

Table A.1. Best-fitting parameters from the HFS method in GILDAS applied to the N_2H^+ spectra towards the core G3.

From these parameters, we estimate the excitation temperature using the following equation (e.g. Punanova et al. 2016):

$$T_{ex} = \frac{h\nu}{k}\left[ln\left(\frac{(h\nu/k)}{(T_A \times \tau)/\tau + J_\nu(T_{bg})} + 1\right)\right]^{-1}, \quad (A.1)$$

where ν is the frequency of the component used as a reference in the HFS fitting; $J_\nu(T_{bg})$ is the equivalent Rayleigh-Jeans background temperature (T_{bg}=2.73 K); and τ is the optical depth of the main component. In the case of optically thick lines, $T_A \times \tau$ is the total optical depth times the difference between the Rayleigh-Jeans equivalent excitation and background temperatures, while for the case of optically thin lines it corresponds to the main beam temperature of the main component. From Equation A.1, we estimate the excitation temperature to be T_{ex}=7 K. This value is consistent with that reported in other low-mass (Friesen et al. 2013) and high-mass cores (Fontani et al. 2011; Kong et al. 2016) and towards other IRDCs (Barnes et al. 2016). Assuming T_{ex}=7 K would lead to $D_{frac}^{N_2H^+}$ values lower by less than 10% with respect to those reported in Table 3 for T_{ex} = 9 K.